JOURNAL OF SPACECRAFT AND ROCKETS
Vol. 44, No. 4, July–August 2007

Aerothermodynamic Optimization of Reentry Heat Shield Shapes for a Crew Exploration Vehicle

Joshua E. Johnson,* Ryan P. Starkey,† and Mark J. Lewis‡
University of Maryland, College Park, Maryland 20742

DOI: 10.2514/1.27219

Gradient-based optimization of the aerodynamic performance, static stability, and stagnation-point heat transfer was performed to obtain optimal heat shield geometries for blunt-bodied planetary entry vehicles. Cross sections considered include oblate and prolate ellipses, rounded-edge polygons, and rounded-edge concave polygons. Axial profiles consist of the spherical segment, spherically blunted cone, and power law. Aerodynamic models are based on modified Newtonian impact theory with semi-empirical shock-standoff distance and heat transfer correlations. Methods were verified against wind-tunnel and flight data of the Apollo Command Module and Fire 2; they are within 12% for aerodynamic coefficients and stagnation-point heat fluxes. The selected design point corresponds to the setting in which the Apollo 4 Command Module generated its maximum heat flux, at an altitude of 61 km and a velocity of 10.3 km/s. Results indicate that oblate parallelogram configurations provide optimal sets of aerothermodynamic characteristics.

Nomenclature

A	=	coefficient of the power law
b	=	exponent of the power law
C	=	aerodynamic coefficient
d	=	diameter, m
e	=	eccentricity
$\boldsymbol{G}$	=	optimization constraints vector
g_1, g_2, g_3	=	radiation correlation parameters
g_w	=	ratio of wall enthalpy to total enthalpy
H	=	correlation exponent
h	=	altitude, km
j	=	semimajor axis length of a blunt body, m
k	=	semiminor axis length of a blunt body, m
l	=	length of heat shield from nose to base, m
L/D	=	lift-to-drag ratio
M_∞	=	freestream Mach number
m	=	number of sides of the superellipse in the superformula
n_1, n_2, n_3	=	superelliptic parameters
Q	=	heat load, J/cm^2
q_∞	=	freestream dynamic pressure, Pa
q	=	heat flux, W/cm^2
r	=	base radius, m
r_{eff}	=	effective radius of curvature for radiative heat transfer, m
r_n	=	nose radius for the spherically blunted cone axial profile, m
r_s	=	radius of curvature for the spherical-segment axial profile, m
S	=	surface area of cross section, m^2
V_∞	=	freestream velocity, m/s
v, w	=	superellipse parameters
$\boldsymbol{X}$	=	design variables vector
X	=	x location, m
x, y, z	=	coordinate values
α	=	angle of attack, deg
β	=	sideslip angle, deg
γ	=	ratio of specific heats
Δ_{so}	=	shock-standoff distance, m
ε	=	edge tangency angle, deg
η_v	=	volumetric efficiency
θ_c	=	half-cone angle, deg
θ_s	=	half-spherical-segment angle, deg
ρ	=	density, kg/m^3
ϕ	=	sweep angle, rad

Subscripts

A	=	axial force
cg	=	center of gravity
conv	=	convective
cp	=	center of pressure
D	=	drag
H	=	horizontal component with respect to the body
L	=	lift
l	=	rolling moment
m	=	pitching moment
max	=	point of maximum heat transfer
N	=	normal force
n	=	yawing moment
rad	=	radiative
s	=	stagnation point
sl	=	sea level
tot	=	total
V	=	vertical component with respect to the body
Y	=	side force
α	=	derivative with respect to angle of attack, rad
β	=	derivative with respect to sideslip angle, rad
1	=	before the normal shock
2	=	after the normal shock
∞	=	freestream

Presented as Paper 6273 at the AIAA Atmospheric Flight Mechanics Conference and Exhibit, Keystone, CO, 21–24 August 2006; received 10 August 2006; revision received 22 December 2006; accepted for publication 25 January 2007.

*Graduate Research Assistant, Department of Aerospace Engineering, 3181 Glenn L. Martin Hall; johnsje@umd.edu. Student Member AIAA.

†Research Scientist, Department of Aerospace Engineering, 3181 Glenn L. Martin Hall; rstarkey@umd.edu. Senior Member AIAA.

‡Professor, Department of Aerospace Engineering, 3181 Glenn L. Martin Hall; lewis@eng.umd.edu. Fellow AIAA.

I. Introduction

PLANETARY entry vehicles require a proper combination of aerodynamic performance, stability, and heat transfer to successfully follow an entry trajectory. The simplest blunt-bodied

planetary entry vehicle is the reentry space capsule. Blunt-bodied capsules, such as the one that will be used by NASA's Orion crew exploration vehicle (CEV), will reenter Earth's atmosphere at high hypersonic velocities, with projected Mach numbers ranging from 30 to 50. Such high Mach numbers deliver very high heat loads along the frontal surface. It is the aim of this work to examine several optimized heat shield geometries, accounting for aerodynamics, static stability, and heat flux. A priori, it is not clear that the classic spherical segment [1] or spherically blunted cone [2,3] provides optimal aerothermodynamic performance. Executing an optimization of a broad range of heat shield shapes may assist in ascertaining a more optimal configuration with a higher lift-to-drag ratio L/D and a lower heat transfer flux. A parametric formulation of the aerodynamic performance and stability of heat shields based on Newtonian impact theory was completed previously [4] and serves as the foundation of the present work. That analysis was augmented with the addition of semi-empirical methods for the calculation of convective and radiative stagnation-point heat fluxes. The contributions of viscous shear forces are not considered in this analysis. Together with the software package Design Optimization Tools (DOT), the aerothermodynamics of several heat shield geometries are evaluated to identify optimal configurations.

Despite decades of experience, blunt-bodied reentry geometries still have unknown characteristics, and this work seeks to impart greater understanding of the performance for a broad range of possible designs. This work is relevant because inconsistencies and poor assumptions were observed throughout the literature, both recently and in the past. One such discrepancy concerns locating the center of pressure. The previous work [4] addressed the theory behind this issue and included validation of its method by matching Project Apollo's $C_{m,\mathrm{cg}}$ wind-tunnel data and trim angles of attack. This present optimization accounts for these and other issues mentioned in [4].

This work is divided into four sections:

1) Heat shield geometries are introduced to demonstrate the wide range of common and unique geometries available in the design space.

2) Additions to the previous work [4], including methods for determining heat flux values, are referred to and validated against the Apollo 4 and Fire 2 flight tests.

3) The setup for the optimization is given, comprising optimization methodology, chosen objective functions, design variables, and design space constraints.

4) The results of the optimization are examined, and optimal heat shields are compared with the Apollo heat shield.

II. Methodology and Validation

It is assumed that the hypersonic aerothermodynamic performance for a reentry capsule is mainly defined by the heat shield's geometry. The aerodynamic analysis of each heat shield is performed using modified Newtonian flow on a widely variable parametric geometry generator. It was shown in previous work [4] that a modified Newtonian surface pressure distribution is acceptable for estimating the aerodynamic performance of the Apollo Command Module (CM) at high planetary entry velocities and trim angles of attack, for entry from both Earth orbit and from lunar return. Validation results from [4] are within 10% for aerodynamic coefficients, and trim angles of attack are computed within 1.2-deg. Modified Newtonian flow theory is applied to an initial analysis of other similar hypersonic blunt-body designs.

A. Heat Shield Shapes

The heat shield geometry is defined by two contours (the base cross section of the heat shield and the axial profile that is swept about the central axis) and tailored to match the base cross section. For gradient-based optimization, the ideal equation defining the geometry would produce a wide, continuous range of cross sections. One such equation is available using the superformula [5] of the superellipse. It defines the cross-sectional radius for $0 \le \phi \le 2\pi$:

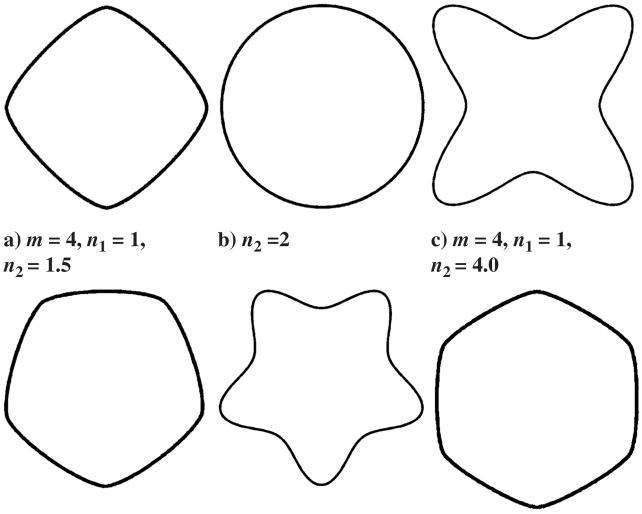

a) $m = 4, n_1 = 1, n_2 = 1.5$ **b)** $n_2 = 2$ **c)** $m = 4, n_1 = 1, n_2 = 4.0$

d) $m = 5, n_1 = 1.75, n_2 = 1.5$ **e)** $m = 5, n_1 = 1.75, n_2 = 4.0$ **f)** $m = 6, n_1 = 1.75, n_2 = 1.5$

Fig. 1 Examples of base cross sections.

$$r(\phi) = \left[\left|\frac{\cos(\frac{1}{4}m\phi)}{v}\right|^{n_2} + \left|\frac{\sin(\frac{1}{4}m\phi)}{w}\right|^{n_3}\right]^{-1/n_1} \tag{1}$$

where m corresponds to the number of sides of a polygon, $v = w = 1$, n_1 and n_2 are modifiers, and $n_3 = n_2$ to render sharp or rounded-edge polygons. Increasing n_2 transforms a polygon ($n_2 < 2$) into an ellipse ($n_2 = 2$) and then into a rounded-edge concave polygon ($n_2 > 2$). Example cross sections are shown in Fig. 1, and the ranges of values used in this work for parameters m, n_1, and n_2 are listed Table 1. Note that Fig. 1b shows the ellipse generated by Eq. (1) with $n_2 = 2$, independent of n_1 and the chosen type of polygon.

Once the cross section is chosen, the axial profile, or shape of the heat shield that protrudes from the base, is selected. Three axial profiles are considered: the spherical segment, the spherically blunted cone, and the power law. To generate a heat shield geometry, the axial profile is rendered and then swept 360 deg about the central body axis using Eq. (1), based on the selected cross-sectional contour.

Figures 2 and 3 show the spherical-segment and spherically blunted cone geometries, respectively. The power-law formula $y = Ax^b$ offers axial profiles with a wide range of bluntness being controlled by coefficient A and exponent b, as shown in Figs. 4a and 4b, respectively. The fixed-body coordinate system for this work is included in Fig. 2.

In the fixed-body coordinate system, it is the convention to combine the three orthogonal force vectors $\boldsymbol{C}_A$, $\boldsymbol{C}_N$, and $\boldsymbol{C}_Y$ into the two aerodynamic force vectors $\boldsymbol{C}_L$ and $\boldsymbol{C}_D$. Lift is divided into vertical and horizontal components (with respect to the z axis), represented by L_V and L_H, respectively, for the cases with $\beta \neq 0$. In calculating rolling moment stability, the sign of L_V determines the direction of the positive rolling moment, shown in Fig. 2. Even though L_H is negligible in this particular analysis, because β is small

Table 1 Superformula parameters for rounded-edge polygons ($n_3 = n_2$)

m	n_1	n_2
4	1.00	1.3–4.0
5	1.75	1.3–4.0
6	2.30	1.3–4.0
7	3.20	1.3–5.0
8	4.00	1.3–6.0
9	5.50	1.3–6.0
10	7.00	1.3–7.0

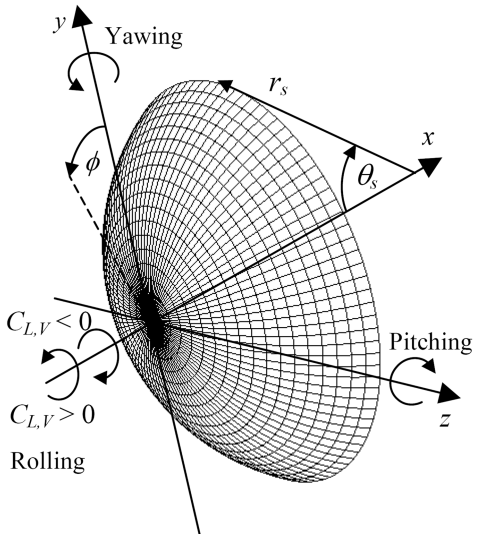

Fig. 2 Spherical segment; $\theta_s = 60$ deg and $n_2 = n_3 = 2$.

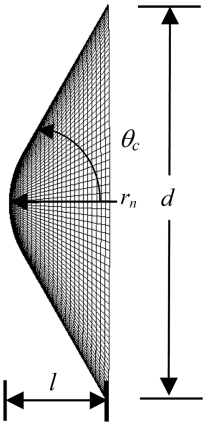

Fig. 3 Spherically blunted cone axial profile; $r_n/d = 0.25$ and $\theta_c = 60$ deg.

compared with α, L_V is listed in the results to be consistent with general theory and previous work [4]. This allows the definition of static roll stability, $C_{l,\mathrm{cg},\beta} < 0$, to remain constant. The moment coefficients are defined as the ratio of the moment to $q_\infty S l_M$, in which l_M is defined as the length of the semimajor axis of the base cross section [4]. Additional details of both the static stability and the heat shield shapes in this work are given in [4].

B. Heat Transfer Calculations and Validation

The convective and radiative stagnation-point heat fluxes are determined using heat transfer correlations for Earth. The only geometric parameter that convection is dependent upon is the nose radius of the blunt body. The convection correlation [6] is

$$q_{s,\mathrm{conv}} = (1.83 \times 10^{-8}) r_n^{-0.5} (1 - g_w) \rho_\infty^{0.5} V_\infty^3 \tag{2}$$

where this work assumes that $g_w \ll 1$.

Because radiation over a blunt body can be primarily modeled as an elliptic problem, stagnation-point radiative heat transfer depends on the shape of the vehicle, in addition to the nose radius term. It is also sensitive to the angle of attack of the blunt body. All of these factors are incorporated into an effective radius term r_{eff}. Because correlations for $q_{s,\mathrm{rad}}$ are available for a sphere with a given radius, the effective radius is directly related to the sphere's radius, to apply the correlations to nonspherical blunt bodies. This is accomplished by relating the shock-standoff distance to both radii.

This method is based on the assumption that the effective radius for radiative heat transfer r_{eff} is equal to the radius of that particular sphere that maintains an equal shock-standoff distance Δ_{so} normal to the stagnation point at a given normal shock density ratio ρ_2/ρ_1. According to wind-tunnel results [7], the normal shock-standoff distance for a sphere of radius r_{eff} is constant for a given normal shock density ratio, and an empirical curve fit renders the following approximation:

$$\Delta_{\mathrm{so}}/r_{\mathrm{eff}} = \left(\frac{[(\rho_2/\rho_1) - 1]^2}{(\rho_2/\rho_1) - \sqrt{(2\rho_2/\rho_1) - 1}} - 1 \right)^{-1} \tag{3}$$

The normal shock density ratio and specific heat ratio are determined by iterating the Tannehill and Mugge [8] high-temperature-correlation set until the ratio of specific heats γ converges. Then the shock-standoff distance is calculated by the semi-empirical method of Kaattari [9,10] for the chosen angle of attack. Kaattari and others [11] validated his method for the spherical segment and spherically blunted cone at zero angle of attack [9], and it was validated for the spherical segment at nonzero angles of attack [10,11]. Once ρ_2/ρ_1 and Δ_{so} are determined, the effective radius can be calculated from Eq. (3). Then the r_{eff} replaces the spherical radius in the correlations for $q_{s,\mathrm{rad}}$.

As part of the validation of Kaattari's [9,10] method, normalized values of Δ_{so} for a sphere are plotted in Fig. 5 against those of Eq. (3), as well as the vorticity method and parabolic thin-shock-layer approximation [12]. The wind-tunnel results [7] lie within the bounds of the empirical equation (3) and Kaattari's method and are closer to Kaattari's method for density ratios below 12.

Two $q_{s,\mathrm{rad}}$ correlations are applied over a range of freestream velocities. For $V_\infty < 9000$ m/s, the correlation of the following form is applied:

$$q_{s,\mathrm{rad}} = r_{\mathrm{eff}} g_1 (3.28084 \times 10^{-4} V_\infty)^{g_2} (\rho_\infty/\rho_{\mathrm{sl}})^{g_3} \tag{4}$$

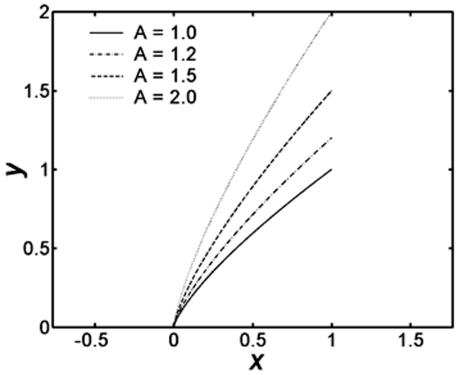

a) Cross sections of power law varying A, $b = 0.75$

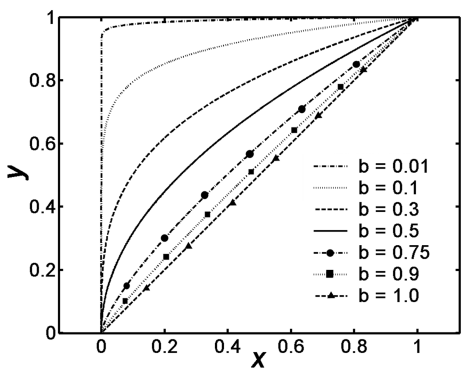

b) Cross sections of power law varying b, $A = 1$

Fig. 4 Power-law axial profile.

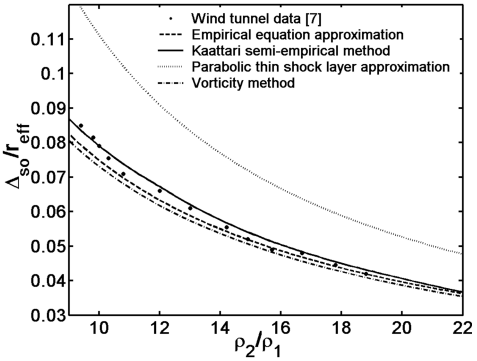

Fig. 5 Normalized shock-standoff distance, varying with normal shock density ratio.

where $g_1 = 372.6$, $g_2 = 8.5$, and $g_3 = 1.6$ from [13] for $V_\infty <$ 7620 m/s; and $g_1 = 25.34$, $g_2 = 12.5$, and $g_3 = 1.78$ from [14] for velocities of 7620 to 9000 m/s. For velocities above 9000 m/s, the Tauber and Sutton [15] equation is applied:

$$q_{s,\text{rad}} = 4.736 \times 10^4 r_{\text{eff}}^H \rho_\infty^{1.22} f(V_\infty) \tag{5}$$

where $H = 1.072 \times 10^6 V_\infty^{-1.88} \rho_\infty^{-0.325}$, and

$$f(V_\infty) = \begin{cases} -3.93206793 \times 10^{-12} V_\infty^4 + 1.61370008 \times 10^{-7} V_\infty^3 - 2.43598601 \times 10^{-3} V_\infty^2 & \\ +16.1078691 V_\infty - 39,494.8753 & 9000 \le V_\infty \le 11,500 \text{ m/s} \\ -1.00233100 \times 10^{-12} V_\infty^4 + 4.89774670 \times 10^{-8} V_\infty^3 - 8.42982517 \times 10^{-4} V_\infty^2 & \\ +6.25525796 V_\infty - 17,168.3333 & 11,500 < V_\infty \le 16,000 \text{ m/s} \end{cases}$$

The curve-fit equations for $f(V_\infty)$ have a high number of significant figures, resulting in less than 2% error with the published tabulated values [15]. It is suggested that all of these significant figures are maintained; if they are not, the values of $f(V_\infty)$ may go below zero for low V_∞ or produce extremely large values for high V_∞, either case producing erroneous results. The high number of significant figures does not correspond to the resultant number of significant figures from this correlation. It is suggested that no more than three digits should be specified as significant for both radiative heat flux correlations. Note that $H = 1$ must always be met.

For validation of this method of calculating the stagnation-point radiative heat flux, the heating of the Apollo CM geometry at $\alpha = -25$ deg, based on the freestream coordinate system in Fig. 6, along the Apollo 4 trajectory [16] shown in Fig. 7, is compared with the Ried et al. [7] Apollo 4 predictions (as well as other correlations [13–15,17]) in Fig. 8, using $r_{\text{eff}} = 2.9$ m. Note that the $q_{s,\text{rad}}$ correlation from Bertin [13] was expected to be less accurate for this flight regime, because it was applied above its designed upper limit on V_∞, equal to satellite velocity ($V_\infty = 7900$ m/s). Ried et al. generated $q_{s,\text{rad}}$ predictions for Apollo 4 with early 1970 computer technology using computational fluid dynamics (CFD). Equation (5) from Tauber and Sutton [15] most closely follows the Apollo 4 prediction curve. The Apollo 4 also had radiometer data, but it only measured the visible and infrared radiation intensities, leaving the UV radiation intensity values unknown [18]. However, the breakdown of the Apollo 4 predictions follows most of the flight data, thus the radiative heat flux correlations are compared with the overall predictions with confidence.

Ried et al. [7] also calculated an effective radius that varies with α, and it is compared in Fig. 9 to the results of this work, which applies Kaattari's [9,10] modified method. This work varies no more than 10% from the Ried et al. predictions. In the present work, once r_{eff} is

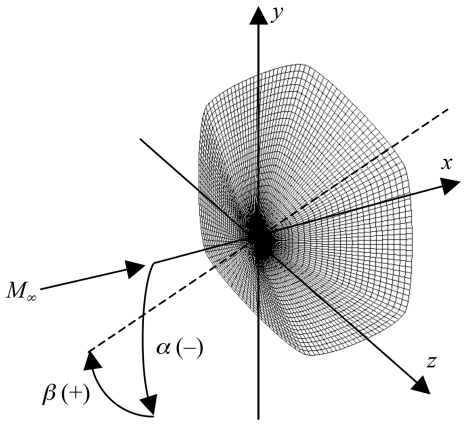

Fig. 6 Freestream coordinate system.

calculated, it is applied to the radiative heat flux correlation set. For validation, this process is completed for each specified point along the Apollo 4 trajectory, to computer a total heat load.

To validate the convective heat flux, radiative heat flux, and the corresponding heat load values, results were generated using the Apollo 4 trajectory. Apollo 4 had the highest entry velocity of all Apollo missions, equal to 10.7 km/s, which is equivalent to $M_\infty \approx 40$, and it also had the largest heat load. Using two different $q_{s,\text{conv}}$ correlations, Eq. (2) and one from Lovelace [14], and the $q_{s,\text{rad}}$ correlation set, the total heat flux and heat loads are calculated and then compared with previous work in Table 2.

Lee and Goodrich [18] and Pavlosky and Leger [19] reported the values of the heat flux and heat load at the point of maximum heating, which in the case of the Apollo CM was not at the stagnation point, but was instead at the top edge of its heat shield, due to its high angle of attack during reentry. Although this work calculates the stagnation-point heating, the reported values in [18,19] can still be used for validation. The maximum convective heating for the Apollo CM at $\alpha = -25$ deg was 60% larger than the stagnation-point

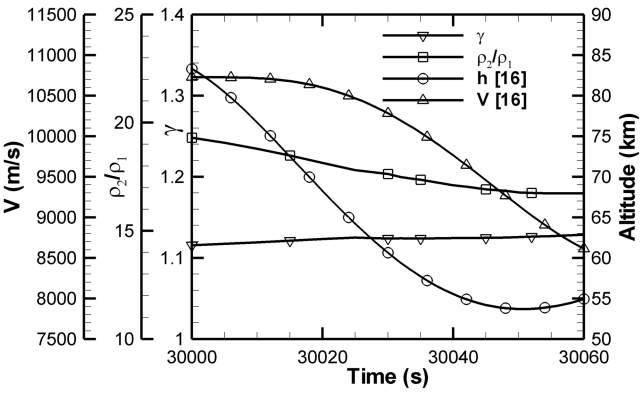

Fig. 7 Normal shock density ratio and specific heat ratio, with altitude and velocity histories of Apollo 4 reentry.

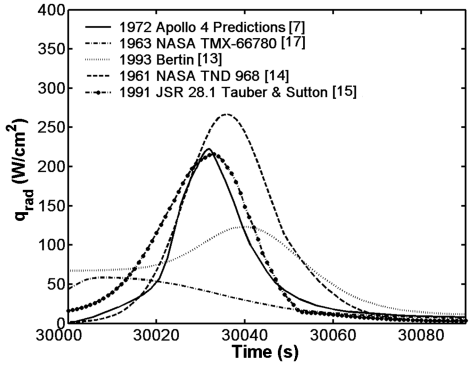

Fig. 8 Radiative heat flux of Apollo 4; correlation comparison with predictions.

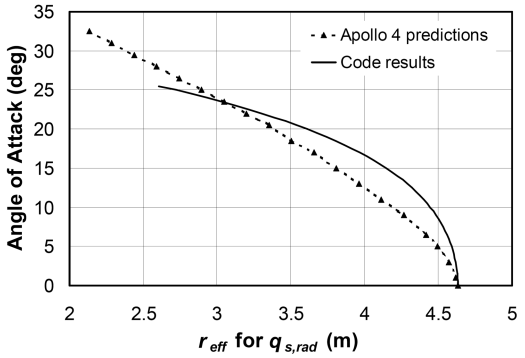

Fig. 9 Apollo 4 CM r_{eff} comparison with [7].

convective heat flux [18] at zero angle of attack, and Bertin [13] notes that a correction factor of 1.06 to the correlation for a sphere can be applied to account for the change in the sonic line location from 45 deg for a sphere to approximately 25 deg for the CM. In this way, the stagnation-point convective heat flux could be multiplied by both 1.6 and 1.06 and then added to the radiative heat flux to approximate the maximum heat flux and heat load. The results in Table 2 are within 12% of the reported values.

The Fire 2 experiment entered Earth's atmosphere at 11.4 km/s and had three heat shields of different radii (0.94 m, 0.80 m, and 0.70 m) placed on top of each other. After heat transfer data were acquired for a heat shield, it was jettisoned, leaving the subsequent heat shield in the freestream flow. Because the heat shields have different radii, discontinuities in the flight data and theory curves are expected. As shown in Fig. 10, flight data from the calorimeter [20] produced a smaller heat flux value than the curve based on theory without convective–radiative coupling. The correlations of this work, which are labeled as code results, also do not assume coupling. The calorimeter flight data have a peak value of 1140 W/cm^2 at an altitude of 50.7 km and a velocity of 10.2 km/s. The code generated 1220 W/cm^2 (+7% difference), which is closer to the calorimeter data than the uncoupled theory that calculated 1320 W/cm^2 (+16% difference). The convective theory curve assumes that coupling and the code results match nearly perfectly for the first shield and do not vary greatly for the other two. However, it is apparent that this work falls approximately halfway between the theory that assumes no coupling and the calorimeter data. It is believed that the Fire 2 experiment experienced some convective–radiative coupling, and that this may be the reason that the total heat flux theory without coupling and the code results produce a peak at a time different from

Table 2 Apollo 4 comparison of total heat transfer

Parameters	Apollo 4 [19]	Results with $q_{s,\text{conv}}$ from [14], % error	Results with Eq. (2), % error
$q_{\max,\text{tot}}$, W/cm^2	480	540 (+12%)	470 (−2.1%)
$Q_{\max,\text{tot}}$, J/cm^2	42,600	46,200 (+8.5%)	38,700 (−9.2%)

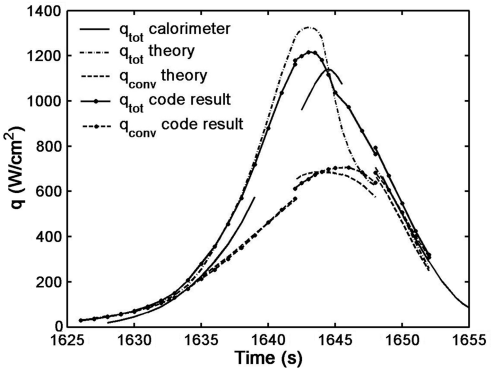

Fig. 10 Fire 2 $q_{s,\text{tot}}$ with flight data from [20].

the Fire 2's calorimeter data. As a result, it would be expected that this work's accuracy would begin to disappear at slightly higher velocities in which coupling effects become more significant.

Note that the blunt bodies with a power-law axial profile must have an equivalent nose radius term to apply these heat transfer correlations (calculated using methods described in [21]). This is due to the fact that a power-law body may have a sharp nose. The equivalent nose radius in this work is only an approximation and should not be accepted as a complete model for power-law shapes.

C. Optimization Setup

The parametric study [4] indicated that the design space of the aerodynamics and static stability of these configurations is primarily continuous. For that reason, a gradient-based optimization method is applied in this work. To find optimal heat shield designs, Vanderplaats Research & Development, Inc.'s DOT software [22] is used in conjunction with the aerothermodynamics code written for this work. DOT is a software package that varies design variables using gradient-based minimization to determine an optimum value for a given objective function. The gradient-based optimization method known as the modified method of feasible directions (MMFD) included in DOT is applied, because it is the most reliable of the three and requires less memory than the other two methods [22]. Detailed descriptions of MMFD and the Kuhn–Tucker conditions required for convergence are included in Appendix E of [22].

Aerothermodynamic characteristics considered for optimization consist of L_V/D, $q_{s,\text{tot}}$, and $C_{m,\text{cg},\alpha}$. An optimal lift-to-drag ratio minimizes g loads and maximizes controllability, cross range, and downrange. An optimal $q_{s,\text{tot}}$ minimizes the temperatures experienced during reentry and minimizes its integrated heat load. Because this optimization is executed only at a single design-point location along a representative trajectory, trajectory analysis is not included, and the heat load is not considered. For this case, the optimal $q_{s,\text{tot}}$ for a single design point would have the lowest value. An optimal $C_{m,\text{cg},\alpha}$ maximizes longitudinal stability and controllability. Similar to aircraft stability, a value of $C_{m,\text{cg},\alpha}$ with a high magnitude can reduce controllability, and an analysis of the required static stability for entry vehicles would be a topic for future work. In this work, the static stability of optimal configurations is compared with the Apollo Command Module's stability characteristics.

Collectively, an optimal set of aerothermodynamic characteristics at a single design point along a representative trajectory would consist of a high L_V/D, a low $q_{s,\text{tot}}$, and a $C_{m,\text{cg},\alpha} < 0$ with a high magnitude. This analysis is completed by using single-objective function optimization, and the objective functions chosen for this analysis consist of maximizing L_V/D and of minimizing $q_{s,\text{tot}}$ and $C_{m,\text{cg},\alpha}$. Because a configuration with a high L_V/D may not experience a low $q_{s,\text{tot}}$, maximizing $(L_V/D)/q_{s,\text{tot}}$ is also considered, because this objective function is designed to provide a compromise between a high L_V/D and a low $q_{s,\text{tot}}$. Similar tradeoffs between other ideal characteristics also exist.

A separate optimization is run for each of the three axial profiles. For each profile, the design variables with their lower and upper

Table 3 Design variables with side constraints for each axial profile

Spherical segment	Spherically blunted cone	Power law
	$55.0\,\text{deg} \le \theta_c \le 89.0\,\text{deg}$	$0.200 \le b \le 0.999$
$5.0\,\text{deg} \le \theta_s \le 89.0\,\text{deg}$	$0.15 \le r_n/d \le 2.00$	$0.900 \le A \le 10.000$
$1.30 \le n_2 \le 4.00$	$1.30 \le n_2 \le 4.00$	$1.30 \le n_2 \le 4.00$
$-0.968 \le e \le 0.968$	$-0.968 \le e \le 0.968$	$-0.968 \le e \le 0.968$
$-30\,\text{deg} \le \alpha \le 30\,\text{deg}$	$-30\,\text{deg} \le \alpha \le 30\,\text{deg}$	$-30\,\text{deg} \le \alpha \le 30\,\text{deg}$

constraint values are given in Table 3. For the spherical-segment geometries, the lower limit of $\theta_s = 5$ deg provides a blunt body that has a high, but finite, radius of curvature, and the upper limit of 89 deg removes numerical issues that exist if the upper limit is set to 90 deg for both θ_s and θ_c. Additionally, zero radius of curvature designs are not considered, because they produce high heat concentrations. In generating the base cross section, the lower limit of the transformation variable n_2 is 1.3, to produce slightly rounded-edge polygons. As n_2 is increased, the polygon's edges become more rounded, and the polygon is completely transformed into an ellipse at $n_2 = 2.0$. Increasing n_2 further transforms the ellipse into a rounded-edge concave polygon. An upper limit of four on n_2 was chosen arbitrarily to restrict Eq. (1) from generating cross sections with an extremely low reasonable radius of curvature.

The maximum eccentricity of ± 0.968 was chosen to limit the axes ratio j/k to less than or equal to four. The angle of attack is limited to ± 30 deg because manned space capsules usually enter at or below $|\alpha| = 25$ deg and also due to the fact that the heat shield may not be even half of the vehicle's shape. If θ_s is large, then it is possible that the entire space capsule could fit within a hard- or soft-shell reentry system, including inflatable aeroshell devices.

A noneccentric heat shield with $\theta_c \approx 45$ deg is the interface at which the spherically blunted cone begins to produce positive L_V at negative α [23]. If $\theta_c \le 45$ deg, then negative L_V is generated at negative α. The term *blunt body* for reentry commonly refers to a vehicle that produces a bow shock with a substantial standoff distance. Because Ried et al. [7] approximated that the shock-standoff distance of the Apollo 4 was 14 cm and this work predicts 12.4 cm ($M_\infty = 32.8$ and $\alpha = 25$ deg at $h = 61$ km, at 30,030 s into the mission), it was decided that the order of accuracy of Kaattari's [9,10] method is approximately 2.54 cm. As a result, the characteristics of the spherically blunted cone that has a shock-standoff distance of 2.54 cm would represent the lower limit for θ_c and r_n/d. For a noneccentric heat shield, this work predicts a 2.54-cm shock-standoff distance for a spherically blunted cone with $\theta_c = 55$ deg and $r_n/d = 0.25$. The lower limit on the nose radius-to-diameter ratio is not greater than 0.25, because previous work such as the Mars Viking missions included heat shields with $r_n/d = 0.25$. The chosen lower limit of $r_n/d = 0.15$ widens the design space. The upper limit to r_n/d is set at two, to include some geometries that are pure spherical segments.

For the power-law designs, Newtonian impact theory may have an accuracy issue, given the quick slope changes shown in Fig. 4b for $b = 0.1$ or smaller, and so the lower limit value of 0.2 for b was chosen arbitrarily. The upper limit on b produces a nearly linear profile, but the code requires the slope of the power-law profile to vary at least slightly, for numerical reasons. Because blunt bodies in previous work usually have $l < d$ (i.e., Apollo CM had $l/d \approx 1/9$), it was decided in this work to widen the design space by including $A = (l/d)^{-1} = (10/9)^{-1}$. Then the upper limit $A = 10$, at which the power law becomes similar to the spherical-segment axial profile, was chosen, because it is no longer unique. These limits can be modified in future work.

This optimization uses the following constraint vector $\boldsymbol{G}$

$$\boldsymbol{G} = \{ G_1 \quad G_2, \quad G_3, \quad G_4, \quad G_5 \} = \left\{ \begin{array}{l} -1 + \frac{|\alpha|}{|\varepsilon + 1\,\text{deg}|}, \quad \frac{1}{100}\left(1 + \frac{C_{m,\text{cg},\alpha}}{0.001}\right), \quad \frac{1}{100}\left(1 - \frac{C_{n,\text{cg},\beta}}{0.001}\right), \\ -1 + \ \text{sign}(C_{L,V})\frac{C_{l,\text{cg},\beta}}{0.01}, \quad -1 + \frac{q_{s,\text{tot}}}{3000} \end{array} \right\} \tag{6}$$

where MMFD requires $\boldsymbol{G} \le 0$ for a feasible design. These constraints account for theory limitations (G_1); static longitudinal, directional, and roll stability (G_2, G_3, and G_4); and high heat flux designs (G_5). Because the heat shield shape is not necessarily or usually the entire vehicle shape, a limit on the angle of attack at which a given heat shield can be analyzed must be chosen, to maintain the assumption that the flow generally separates before passing over the aft body (crew compartment). Otherwise, the entire vehicle must be examined initially to determine the hypersonic aerodynamics, because the Newtonian flow assumption $C_p = 0$ for $\boldsymbol{V}_\infty \cdot \hat{n} \ge 0$ would not apply. Constraint G_1 requires that a given heat shield must not be placed at an angle of attack more than 1 deg larger than the heat shield's tangency angle ε, which is the angle produced between the heat shield's edge surface and the vertical axis. In this way, at the limit, the heat shield's edge is normal to the freestream flow when $\alpha = \varepsilon$, and 1 deg above ε was chosen as a small relief factor. When maximizing L_V/D, the optimizer sometimes increases α beyond ε, which leads the optimizer into a region of design space in which the Newtonian flow assumption does not necessarily apply.

G_2 and G_3 are longitudinal and yaw static stability requirements, respectively; because this is a numerical analysis, the magnitude value of 0.001 is deemed significant, rather than 0.000. G_4 is the roll static stability requirement, but it is different from G_2 and G_3 in that it allows for slight instabilities with unstable values up to 0.01/rad to produce heat shields such as the Apollo CM, which is believed to have slight roll static instability with $C_{l,\text{cg},\beta} \approx 0.005/\text{rad}$. This keeps the design space open to successful previous work. The requirement for roll static stability changes sign when $C_{L,V}$ changes sign, as explained in [4], thus requiring a change in the constraint. G_5 provides an upper limit of 3000 W/cm^2 on $q_{s,\text{tot}}$ that is three times the maximum heat flux at which NASA is designing the CEV. Without this limit, maximizing L_V/D or longitudinal static stability results in vehicles with small nose radii that are unrealistic due to their extremely high heat fluxes. Still, this high upper limit allows for designs that will become feasible in the next couple of decades, at least from a stagnation-point heat flux standpoint.

The design-point environment for this analysis corresponds to the setting in which Apollo 4 experienced its greatest total heat flux. This occurred at an altitude of 61 km and a velocity of 10.3 km/s, which is $M_\infty = 32.8$ and $\gamma \approx 1.12$ inside the high-temperature shock layer. Although the aerodynamic performance and static stability characteristics can be given in nondimensional terms, the heat transfer fluxes require the size of the heat shield to be chosen, and so the base diameter of 3.92 m is prescribed, which is equal to that of the Apollo Command Module. Initially, the center of gravity is chosen based on a uniform density distribution. However, results from the parametric analysis [4] show that a longitudinally unstable heat shield could become stable by shifting the center of gravity forward a reasonable amount. The prescribed center of gravity location for these results is equal to that of uniform density, except that the prescribed X_{cg} is set to 75% of the uniform density value of X_{cg}. This allows for a larger feasible design space, with higher lift-to-drag ratios to be accessed.

III. Results

Results are reported for optimal heat shield designs in Tables 4–6, along with the initial design for each optimization run. This analysis is based on a total of 203 optimization runs, each with unique initial design points. The number of sides of the superellipse cross section was considered, and results between geometries with different cross

Table 4 Optimal designs for maximizing L_V/D with different m

Spherical-segment axial profile Initial design $\theta_s = 85.0$ deg, $n_2 = 1.40$, $e = -0.900$, $\alpha = 25$ deg			
m	Optimal design $\theta_s = 89.0$ deg, $e = -0.968$ n_2	 α	Objective function L_V/D
4	1.30	18 deg	1.10
5	1.30	24 deg	0.88
6	2.60	22 deg	0.75
7	1.30	20 deg	0.76
8	1.30	21 deg	0.82

sections are compared. Optimization using each of the three axial profiles was performed, and the engineering global optimum is reported for each objective function in the following sections. More details of this optimization analysis are included in [21]; note that the following results are based on more optimization runs than in [21].

A. Maximizing L_V/D

For the spherical-segment axial profile, Table 4 shows that the vertical lift-to-drag ratio L_V/D is largest for the parallelogram and pentagonal cross sections. The parallelogram cross section ($m = 4$) has the minimum number of sides examined and offers the maximum

Table 5 Aerothermodynamic comparison of maximum L_V/D and minimum $q_{s,\text{tot}}$ designs ($m = 4$); $M_\infty = 32.8$ and $h = 61$ km[a]

	Maximum L_V/D			Minimum $q_{s,\text{tot}}$		
Parameters	SS	SC	PL	SS	SC	PL
	$\theta_s = 89.0$ deg $n_2 = 1.30$ $e = -0.968$ $\alpha = 18$ deg	$\theta_c = 55.0$ deg $r_n/d = 0.15$ $n_2 = 1.30$ $e = -0.968$ $\alpha = 13$ deg	$b = 0.663$ $A = 0.900$ $n_2 = 1.30$ $e = -0.968$ $\alpha = 9$ deg	$\theta_s = 15.9$ deg $n_2 = 4.00$ $e = 0.968$ $\alpha = -12$ deg	$\theta_c = 60.1$ deg $r_n/d = 1.74$ $n_2 = 4.00$ $e = 0.968$ $\alpha = -12$ deg	$b = 0.500$ $A = 7.490$ $n_2 = 1.52$ $e = -0.093$ $\alpha = -12$ deg
$C_{L,V}$	0.53	0.36	0.29	0.27	0.261	0.34
L_V/D	1.10	1.13	2.14	0.20	0.20	0.20
$C_{m,\text{cg},\alpha}$, /rad	−0.235	−0.344	−0.073	−0.068	−0.070	−0.107
$C_{n,\text{cg},\beta}$, /rad	0.125	0187	0.026	0.047	0.047	0.114
$C_{l,\text{cg},\beta}$, /rad	−0.288	−0.298	−0.073	−0.006	−0.006	0.000
$q_{s,\text{tot}}$, W/cm^2	430	520	3000	360	320	340
$q_{s,\text{conv}}$, W/cm^2	240	430	2830	120	130	120
$q_{s,\text{rad}}$, W/cm^2	190	90	170	240	190	220
X_{cp}/l	0.423	0.632	0.570	0.641	0.640	0.660
X_{cg}/l	0.467	0.538	0.520	0.498	0.497	0.496
η_v	61.5%	65.7%	58.0%	48.5%	49.4%	45.0%
Initial designs						
	$\theta_s = 85.0$ deg $n_2 = 1.50$ $e = -0.900$ $\alpha = 25$ deg	$\theta_c = 60.0$ deg $r_n/d = 0.20$ $n_2 = 1.40$ $e = -0.800$ $\alpha = 10$ deg	$b = 0.800$ $A = 1.500$ $n_2 = 1.80$ $e = -0.010$ $\alpha = 20$ deg	$\theta_s = 25.0$ deg $n_2 = 1.30$ $e = -0.800$ $\alpha = -10$ deg	$\theta_c = 60.0$ deg $r_n/d = 2.0$ $n_2 = 3.00$ $e = 0.800$ $\alpha = -12$ deg	$b = 0.350$ $A = 7.000$ $n_2 = 1.50$ $e = -0.100$ $\alpha = -12$ deg

[a]Axial profiles are SS, spherical segment; SC, spherically blunted cone; and PL, power law.

Table 6 Aerothermodynamic comparison of maximum $(L_V/D)/q_{s,\text{tot}}$ and minimum $C_{m,\text{cg},\alpha}$ designs ($m = 4$) with the Apollo Command Module's heat shield; $M_\infty = 32.8$ and $h = 61$ km[a,b]

	Maximum $(L_V/D)/q_{s,\text{tot}}$			Minimum $C_{m,\text{cg},\alpha}$			Apollo
Parameters	SS	SC	PL	SS	SC	PL	SS
	$\theta_s = 89.0$ deg $n_2 = 1.30$ $e = -0.968$ $\alpha = 18$ deg	$\theta_c = 55.0$ deg $r_n/d = 0.24$ $n_2 = 1.30$ $e = -0.968$ $\alpha = 14$ deg	$b = 0.436$ $A = 0.900$ $n_2 = 1.30$ $e = -0.968$ $\alpha = 14$ deg	$\theta_s = 54.0$ deg $n_2 = 2.19$ $e = -0.713$ $\alpha = -3$ deg	$\theta_c = 55.0$ deg $r_n/d = 0.15$ $n_2 = 2.13$ $e = -0.799$ $\alpha = -1$ deg	$b = 0.788$ $A = 0.900$ $n_2 = 2.40$ $e = 0.273$ $\alpha = 0$ deg	$\theta_s = 25.0$ deg $n_2 = 2.00$ $e = 0.000$ $\alpha = -20$ deg
$C_{L,V}$	0.53	0.377	0.43	0.01	0.00	0.00	0.46
L_V/D	1.10	1.07	1.38	0.01	0.00	0.00	0.33
$C_{m,\text{cg},\alpha}$, /rad	−0.235	−0.313	−0.077	−0.335	−0.377	−0.367	−0.153
$C_{n,\text{cg},\beta}$, /rad	0125	0.185	0.024	0.392	0.447	0.359	0.143
$C_{l,\text{cg},\beta}$, /rad	−0.288	−0.289	−0.054	0.007	0.005	0.004	0.005
$q_{s,\text{tot}}$, W/cm^2	430	460	810	400	510	2930	390
$q_{s,\text{conv}}$, W/cm^2	240	340	490	210	430	2810	160
$q_{s,\text{rad}}$, W/cm^2	190	120	320	190	80	120	230
X_{cp}/l	0.423	0.614	0.492	0.597	0.637	0.637	0.656
X_{cg}/l	0.467	0.527	0.484	0.488	0.540	0.537	2.171
η_v	61.5%	66.4%	57.3%	90.8%	84.9%	92.2%	58.3%
Initial designs							
	$\theta_s = 85.0$ deg $n_2 = 1.50$ $e = -0.900$ $\alpha = 25$ deg	$\theta_c = 60.0$ deg $r_n/d = 0.25$ $n_2 = 1.60$ $e = -0.900$ $\alpha = 20$ deg	$b = 0.500$ $A = 1.000$ $n_2 = 1.40$ $e = -0.900$ $\alpha = 10$ deg	$\theta_s = 45.0$ deg $n_2 = 2.00$ $e = 0.300$ $\alpha = 10$ deg	$\theta_c = 55.0$ deg $r_n/d = 1.00$ $n_2 = 2.00$ $e = 0.010$ $\alpha = -20$ deg	$b = 0.300$ $A = 7.000$ $n_2 = 2.00$ $e = 0.500$ $\alpha = -10$ deg	

[a]Axial profiles are SS, spherical segment; SC, spherically blunted cone; and PL, power law.
[b]Apollo configuration is $Y_{\text{cg}}/l = 0.316$ and $Z_{\text{cg}}/l = 0.000$ from [4], with aerodynamics validated.

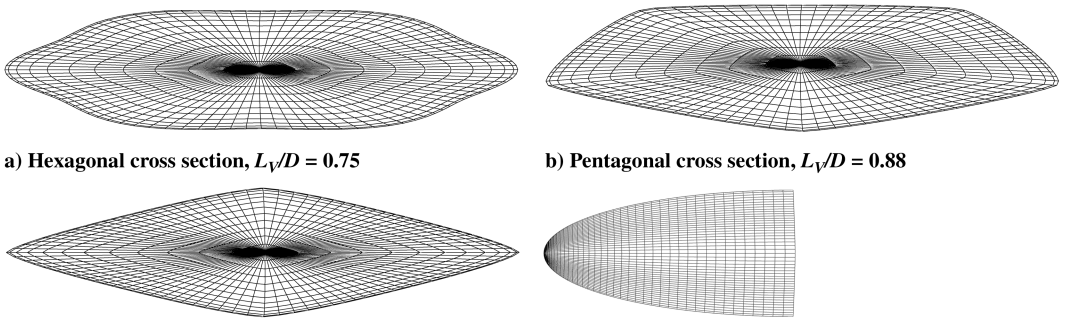

a) Hexagonal cross section, L_V/D = 0.75

b) Pentagonal cross section, L_V/D = 0.88

c) Parallelogram cross section, L_V/D = 1.10

d) Spherical-segment axial profile, θ_s = 89.0 deg

Fig. 11 Optimal geometries from Table 4, $e = -0.968$.

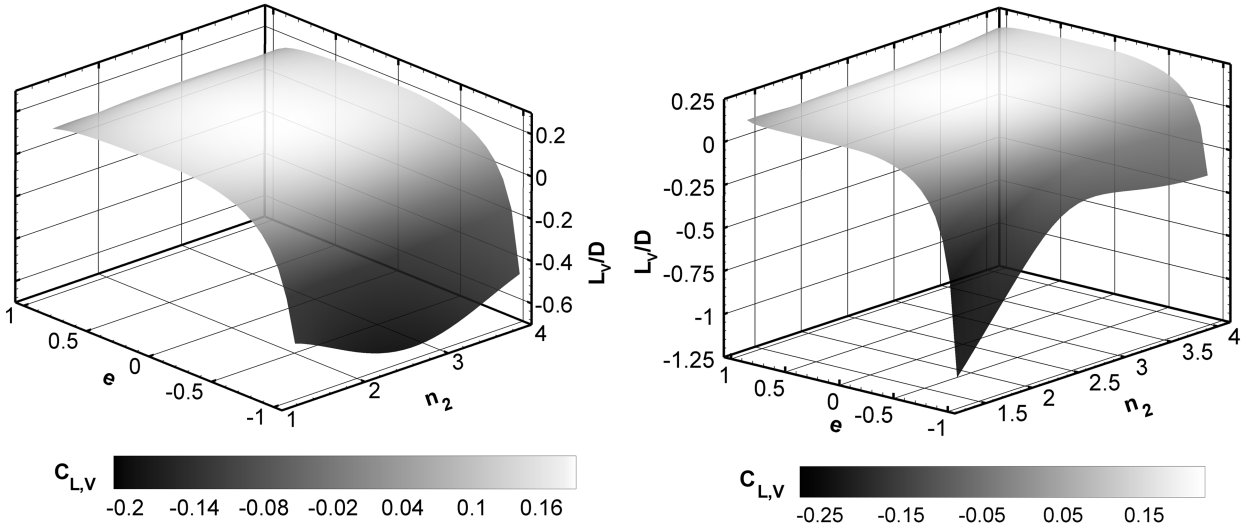

a) Hexagonal base (m = 6)

b) Parallelogram base (m = 4)

Fig. 12 L_V/D distribution for $m = 4$ and 6; spherically blunted cone axial profile; $\theta_c = 55$ deg and $r_n/d = 0.05$; varying e and $n_2 = 1.3$ to 4.0; $M_\infty = 32.8$ and $\alpha = -20$ deg.

lift-to-drag configuration in this analysis. The optimal $m = 4$, 5, and 6 designs are shown in Fig. 11.

The optimal n_2 value for the hexagonal design generates a rounded-edge concave base contour, whereas the other designs do not have concavity. In Fig. 12, the behavior of the hexagonal cross section with a spherically blunted cone axial profile is compared with the parallelogram cross section. The hexagonal design's L_V/D has a maximum magnitude of 0.61, 19% less than its spherical-segment analogue, with an oblate, rounded-edge concave cross section. The parallelogram design's L_V/D continues to increase in magnitude at it approaches the lower endpoint, which is located in the nonconcave region. As a result, varying the hexagonal design produces a different trend from the one generated by varying the parallelogram design. It is only a coincidence that the n_2 value of 2.6 for the hexagonal design in Table 4 is twice that of the other designs with the n_2 lower side constraint active.

The spherical-segment angle constraint is active for the optimal designs with $\theta_s = 89.0$ deg. This high θ_s spherical-segment angle creates geometries that produce positive lift at positive angles of attack, because each has a normal force that contributes more to the lift force than the axial force contributes. For the classic blunt-bodied Apollo Command Module ($\theta_s = 25$ deg), the axial force contributes more to the lift force, thereby requiring a negative angle of attack for positive lift.

For this optimization, the $\boldsymbol{G}$ constraints are neither active nor violated. Because a high L_V/D is desired for several reasons, such as increasing the range of available landing sites and reducing g loads for manned missions, it is one of the most important aerodynamic characteristics of a lifting reentry vehicle. From this point, the optimization analysis is completed with the parallelogram cross section ($m = 4$).

The spherically blunted cone and power-law cases with maximum L_V/D values of 1.14 and 2.14, respectively, are shown in Fig. 13. The actual value of the power law's L_V/D may be lower, because skin friction has not been considered. The optimum power-law geometry has a significant increase in heat transfer flux over the other two geometries, and the heat flux constraint G_5 is active. The power-law shape is allowed to have radii as small as 0.001 m, whereas the spherically blunted cone is restricted to 0.587 m due to limitations in calculating the shock-standoff distance. As a result, only the power-law shape can produce 1000 + W/cm^2 heat fluxes in this work at the given design point using the variable limits listed in Table 3.

The increase in L_V/D is based on the slenderness and different curvature that the power law offers in comparison with the spherical segment. The reason for the power law having an extremely high convective heat transfer flux is due to its small nose radius. Overall, the results in Table 5 are consistent with expected heat transfer trends.

B. Minimizing $q_{s,\text{tot}}$

When changing m to vary the number of sides of the cross section, the resulting minimum $q_{s,\text{tot}}$ values are nearly equal. The configurations with $m = 5$, 6, and 7 have minimum total heat fluxes between 320 and 340 W/cm^2, similar to that of the optimal parallelogram with a spherical-segment axial profile. Table 5 provides the results for minimizing $q_{s,\text{tot}}$ for each of the three axial profiles, and their geometries are shown in Fig. 14. The str'ong

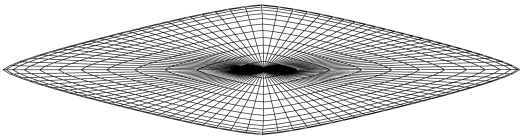

a) Parallelogram cross section, n_2 = 1.30, e = -0.968

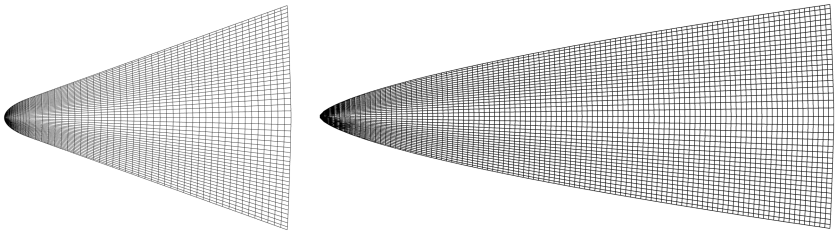

b) Spherically blunted cone axial profile with L_V/D = 1.14

c) Power-law axial profile with L_V/D = 2.14

Fig. 13 Maximum L_V/D geometries from Table 5.

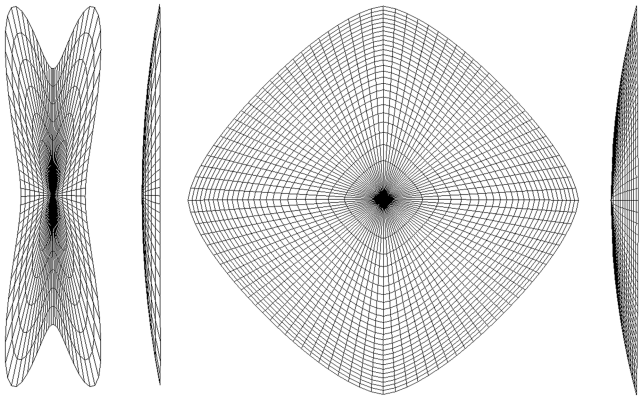

a) Approximated spherical segment and blunted cone designs

b) Power-law design

Fig. 14 Minimum $q_{s,\text{tot}}$ geometries from Table 5.

concavity shown in Fig. 14a may generate corner flow that significantly increases the heat flux experienced in-between the top and bottom cavities. In this respect, this heat shield design is not ideal, and so the value of this result comes solely from the bluntness of the axial profile, which dominantly controls the value of the stagnation-point heat flux.

The high value of r_n/d indicates that the optimal spherically blunted cone is a disguised spherical segment. In this way, the spherically blunted cone axial profile allows the optimization to cover some of the spherical-segment design space. The blunted cone has an $\varepsilon = 16.5$ deg compared with the 15.9 deg of the spherical segment. As a result, these two configurations are nearly identical, and Fig. 14a represents both of them. The Apollo CM's spherical-segment heat shield can be generated with a large nose-radius-to-diameter ratio $r_n/d = 1.18$ and a half-cone angle of 65 deg. Because the minimum $q_{s,\text{tot}}$ blunted-cone configuration actually has a spherical-segment axial profile, the results of this optimization agree with the decision to use a spherical segment instead of the blunted cone for Project Apollo.

Note that although the Apollo 4 CM was traveling at $M_\infty = 32.8$ at 61 km, the manned Apollo Command Modules traveled slower at this altitude, generating less radiative heat flux than experienced during Apollo 4. As a result, a larger radius heat shield would be ideal for this design-point setting, which further supports the use of a spherical-segment heat shield for Apollo.

Although L_V/D is approximately the same for each axial profile, the vertical lift coefficient of the power-law shape without concavity is three times greater than that of the other two. The trend that is suggested from this observation is that if a concave rounded-edge polygon and a rounded-edge polygon have the same L_V/D, the vertical lift coefficient of the rounded-edge polygon may be significantly greater than that of its concave counterpart.

The heat shield with the spherical-segment axial profile has the smallest stagnation-point heat flux, but, because the correlation generated values differ by only 20 W/cm^2, all that can be concluded from these results is that the three axial profiles have approximately the same minimum heat flux value. This work estimates $q_{s,\text{conv}} = 180$ W/cm^2 and $q_{s,\text{rad}} = 210$ W/cm^2 for the Apollo 4 CM at this design point, with $\alpha = -25$ deg. The present work was validated to be within 2.1% of the reported $q_{\max,\text{tot}}$ value of Apollo 4 in Table 2. To reduce the heat flux further, the radius of curvature was increased, resulting in the radiative heat flux dominating over the convective heat flux for this design-point environment. However, note that along a planetary entry trajectory, the convective heat load is expected to dominate over the radiative heat load, as was the case for Apollo 4. In this way, convection is still the primary heat transfer mode.

C. Maximizing $(L_V/D)/q_{s,\text{tot}}$

The spherical-segment configuration with maximum $(L_V/D)/q_{s,\text{tot}}$ is identical to the maximum L_V/D configuration, shown in Fig. 11c, and both were acquired from the same initial design. The optimal designs with blunted-cone and power-law axial profiles are shown in Fig. 15; both posses the same parallelogram base cross section shown in Fig. 15a. The spherically blunted cone cases have nearly identical L_V/D, but the configuration in this optimization, shown in Fig. 15b, has an 11% reduction in $q_{s,\text{tot}}$ from the maximized L_V/D configuration due to its 58% increase in r_n/d. For both configurations to have similar L_V/D values is consistent with one of the conclusions from the parametric analysis [4] that the L_V/D of a blunt body with a high θ_c does not vary greatly with r_n/d. The aerothermodynamic performance and stability characteristics of the heat shield designs with maximum $(L_V/D)/q_{s,\text{tot}}$ are compared with the Apollo Command Module's heat shield in Table 6.

The optimum power-law geometry, shown in Fig. 15b, has the largest L_V/D, equal to 1.39, and a total heat flux of 810 W/cm^2. Note that the stagnation-point heat fluxes for these vehicles can be handled by modern materials such as those that will be used on the Crew Exploration Vehicle, which is being designed to handle 1000 W/cm^2. The shock-standoff distance of the spherically blunted cone is 4 cm, whereas it is calculated to be 37 cm for the power law, although the two nose radii are close in value. This exemplifies the limitations of approximating the power law's nose radius; noneccentric spherical-segment and blunted-cone heat shields were validated against previous work. Their nose radii are determined by definition, whereas a method had to be written for the power-law profile to approximate the nose radius, which is required to use Kaattari's [9,10] method. Note that the total heat flux increases

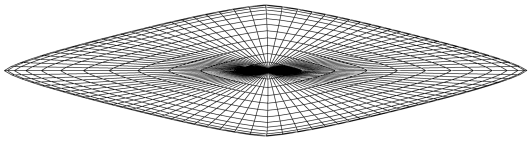

a) Parallelogram cross section, $n_2 = 1.30$, $e = -0.968$

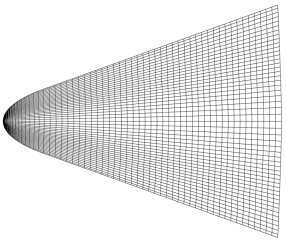

b) Spherically blunted cone axial profile with $L_V/D = 1.07$

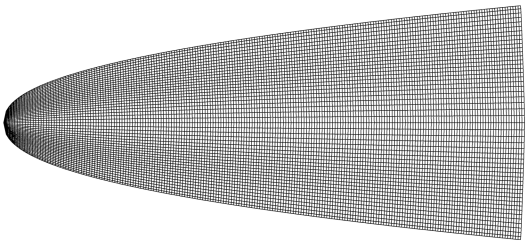

c) Power-law axial profile with $L_V/D = 1.39$

Fig. 15 Maximum $(L_V/D)/q_{s,\text{tot}}$ geometries from Table 6.

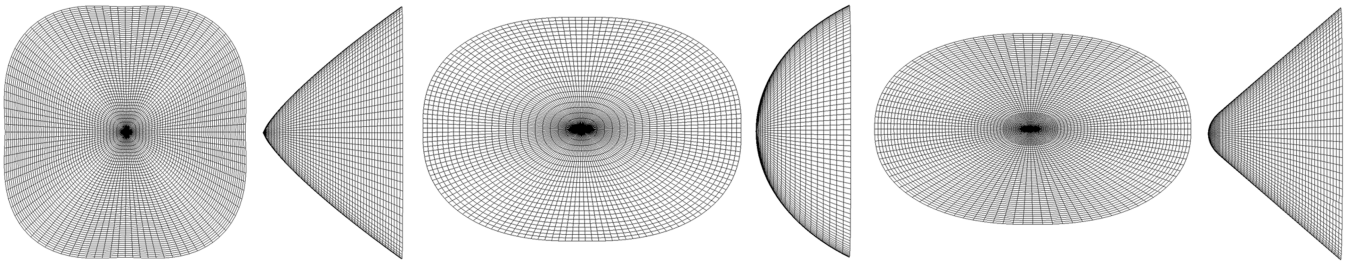

a) Power-law design

b) Spherical-segment design

c) Spherically blunted cone design

Fig. 16 Minimum $C_{m,\text{cg},\alpha}$, geometries ($m = 4$) in Table 6.

with an increase in velocity in a given setting, and the proportions of convective and radiative heat fluxes also change with velocity. As a result, different M_∞ will produce different optimal designs.

D. Minimizing $C_{m,\text{cg},\alpha}$

The pitching moment derivative is commonly the first static stability derivative to be examined. Minimizing the pitching moment derivative $C_{m,\text{cg},\alpha}$ generates negative values with large magnitudes, and the minimum value corresponds to the most statically stable configuration in the longitudinal direction.

The three configurations that are the most statically stable longitudinally are shown in Fig. 16. The optimized power-law geometry has a pointed nose, and the heat flux constraint is close to active at 2910 W/cm^2. The power-law case does not have the eccentricity present in the other two designs, and the spherically blunted cone has a smaller nose radius than the spherical segment. The aerothermodynamic performance and static stability characteristics of these shapes are listed in Table 6. All three shapes have a minimum value of $C_{m,\text{cg},\alpha} \approx -0.30/\text{rad}$.

Note that $-0.30/\text{rad}$ is approximately twice the pitching stability derivative of the Apollo Command Module. The optimum angle of attack for each is near zero. Because these shapes are symmetric about the horizontal fixed-body axis, the lift-to-drag ratio is nearly zero. Similar to the Apollo Command Module, the spherical segment has a slightly unstable rolling moment. Several designs from optimizing the other objective functions have magnitudes of $C_{m,\text{cg},\alpha}$ of less than $0.10/\text{rad}$. As a result, stability and $q_{s,\text{tot}}$ have to be traded off with L_V/D to produce an optimal-set geometry.

IV. Conclusions

Optimization has produced heat shield geometries with improved sets of aerothermodynamic characteristics. Conclusions from optimizing four objective functions include the following.

1) The parallelogram base cross section ($m = 4$) provides the highest L_V/D. Because this is one of the two most important characteristics for a given design-point setting (the other being $q_{\text{max,tot}}$), the optimization was completed primarily with $m = 4$.

2) Minimum heat transfer flux $q_{s,\text{tot}}$ designs may have polygonal bases with and without concavity. However, the concave heat shields may have corner flow that increases the local heat fluxes in the cavities. Further study is required.

3) Two blunt bodies may have the same L_V/D but different $C_{L,V}$. In this case, the rounded-edge, nonconcave polygon has a greater vertical lift coefficient by 300% and thus three times the drag.

4) This work agrees with the decision to use the spherical segment instead of the spherically blunted cone for Project Apollo, strictly from a heat flux standpoint, because minimum $q_{s,\text{tot}}$ configurations have high r_n/d values that are beyond the blunted cone's domain.

5) Designs with maximum static longitudinal stability have values of $C_{m,\text{cg},\alpha}$ that are twice that of the Apollo Command Module.

6) The optimal configurations for L_V/D, $q_{s,\text{tot}}$, and $C_{m,\text{cg},\alpha}$ have tradeoffs with each other. Maximum L_V/D designs have $|\alpha|$ between 8 and 20 deg, whereas a minimum $C_{m,\text{cg},\alpha}$ design has $|\alpha|$ near 0 deg. Additionally, all of the optimum heat shield designs are symmetric about the horizontal axis and thus produce no lift at zero angle of attack. The minimum $q_{s,\text{tot}}$ configurations all had $L_V/D \approx 0.2$, which is lower than the Apollo CM's $L_V/D \approx 0.33$. The power-law design with maximum L_V/D produced a high heat flux, because it is allowed to have a smaller effective nose radius.

7) Maximizing $(L_V/D)/q_{s,\text{tot}}$ resulted in more optimal designs than those produced by optimizing one of the parameters individually. These configurations, which were optimized for an altitude of 61 km and $M_\infty = 32.8$, have the characteristics listed in Table 6. The spherically blunted cone configuration has a pitching stability derivative value of $-0.16/\text{rad}$ that is equivalent to that of the Apollo CM. All of them have high lift-to-drag ratios for planetary entry space capsules, total heat fluxes less than the present NASA CEV requirement of 1000 W/cm^2, and passive static stability.

Acknowledgments

This research was supported by the Space Vehicle Technology Institute (SVTI), one of the NASA Constellation University Institute Projects (CUIP), under grant NCC3-989, with joint sponsorship from the U.S. Department of Defense. Appreciation is expressed to Ken Yu, director of SVTI at the University of Maryland; Claudia Meyer of the NASA John H. Glenn Research Center, program manager of CUIP; and to John Schmisseur and Walter Jones of the U.S. Air Force Office of Scientific Research, whose support is greatly appreciated.

References

[1] Kruse, R. L., Malcolm, G. N., and Short, B. J., "Comparison of Free-Flight Measurement of Stability of the Gemini and Mercury Entry Capsules at Mach Numbers 3 and 9.5," NASA TM-X-957, 1964.

[2] Kirk, D. B., Intrieri, P. F., and Seiff, A., "Aerodynamic Behavior of the Viking Entry Vehicle: Ground Test and Flight Results," *Journal of Spacecraft and Rockets*, Vol. 15, No. 4, 1978, pp. 208–212.

[3] Chrusciel, G. T., and Hull, L. D., "Theoretical Method for Calculating Aerodynamic Characteristics of Spherically Blunted Cones," AIAA Paper 1968-674, June 1968.

[4] Johnson, J. E., Starkey, R. P., and Lewis, M. J., "Aerodynamic Stability of Reentry Heat Shield Shapes for a Crew Exploration Vehicle," *Journal of Spacecraft and Rockets*, Vol. 43, No. 4, July–Aug 2006, pp. 721–730.

[5] Gielis, J., "A Generic Geometric Transformation That Unifies a Wide Range of Natural and Abstract Shapes," *American Journal of Botany*, Vol. 90, No. 3, 2003, pp. 333–338.

[6] Tauber, M. E., and Menees, G. P., "Aerothermodynamics of Transatmospheric Vehicles," *Journal of Aircraft*, Vol. 24, No. 9, 1987, pp. 594–602.

[7] Ried, R. C., Jr., Rochelle, W. C., and Milhoan, J. D., "Radiative Heating to the Apollo Command Module: Engineering Prediction and Flight Measurement," NASA TM X-58091, Apr. 1972.

[8] Tannehill, J. C., and Mugge, P. H., "Improved Curve Fits for the Thermodynamic Properties of Equilibrium Air Suitable for Numerical Computation Using Time-Dependent or Shock-Capturing Methods," NASA CR-2470, Oct. 1974.

[9] Kaattari, G., E., "A Method for Predicting Shock Shapes and Presssure Distributions for a Wide Variety of Blunt Bodies at Zero Angle of Attack," NASA TN D-4539, Apr. 1968.

[10] Kaattari, G., E., "Shock Envelopes of Blunt Bodies at Large Angles of Attack," NASA TN D-1980, Dec 1963.

[11] Walters, E., E., "Free-Flight Measurements of Radiative Heating to the Front Face of the Apollo Reentry Capsule as a Function of Angle of Attack," NASA TM X-851, Feb. 1964.

[12] Rasmussen, M., *Hypersonic Flow*, Wiley, New York, 1994, Chaps. 8, 10.

[13] Bertin, J., *Hypersonic Aerothermodynamics*, AIAA Education Series, AIAA, New York, 1993.

[14] Lovelace, U. M., "Charts Depicting Kinematic and Heating Parameters for a Ballistic Reentry at Speeds of 26,000 to 45,000 Feet per Second," NASA TND-968, Oct. 1961.

[15] Tauber, M. E., and Sutton, K., "Stagnation-Point Radiative Heating Relations for Earth and Mars Entries," *Journal of Spacecraft and Rockets*, Vol. 28, No. 1, 1991, pp. 40–42.

[16] Hillje, E., R., "Entry Aerodynamics at Lunar Return Conditions Obtained from the Flight of Apollo 4 (AS-501)," NASA TN D-5399, 1969.

[17] Lee, D. B., Bertin, J. J., and Ried, R. C., "Apollo Reentry Heating," NASA TM X-66780, Sept. 1963.

[18] Lee, D. B., and Goodrich, W. D., "The Aerothermodynamic Environment of the Apollo Command Module During Superorbital Entry," NASA TN D-6792, Apr. 1972.

[19] Pavlosky, J., and Leger, L., "Apollo Experience Report—Thermal Protection Subsystem," NASA TN D-7564, Jan. 1974.

[20] Cauchon, D. L., "Radiative Heating Results from the FIRE II Flight Experiment at a Reentry Velocity of 11.4 Kilometers per Second," NASA TM X-1402, July 1967.

[21] Johnson, J. E., "Multidisciplinary Optimization of Non-Spherical, Blunt-Body Heat Shields for a Planetary Entry Vehicle," M.S. Thesis, Univ. of Maryland, College Park, MD, 2006.

[22] Design Optimization Tools, Software Package, Ver. 4.20, Vanderplaats Research & Development, Inc., Colorado Springs, CO, 1995.

[23] Davies, C. B., and Park, C., "Aerodynamic Characteristics of Generalized Bent Biconic Bodies for Aero-Assisted Orbital-Transfer Vehicles," NASA TM-84362, 1983.

T. Lin
Associate Editor